Radio Science, Volume ???, Number , Pages 1–20,

Investigation of High-Resolution Microwave Breast Imaging using a 3-D Inverse Scattering Algorithm with a Variable-Strength Spatial Prior Constraint

Luz Maria Neira,[1] Barry D. Van Veen,[1] Susan C. Hagness,[1]

[1]Department of Electrical and Computer Engineering, University of Wisconsin-Madison, Madison, Wisconsin, USA. (e-mail: neira@wisc.edu, vanveen@engr.wisc.edu, hagness@engr.wisc.edu)

Microwave breast imaging is currently being investigated for several clinical applications including evaluation of breast density, detection of breast cancer, and monitoring of treatment. It is a promising alternative to conventional modalities in terms of cost, comfort, and safety. However, the requisite use of regularization techniques to solve the ill-posed inverse scattering problem typically results in moderate imaging resolution. One technique to improve microwave breast imaging resolution is to incorporate *a priori* structural information, also known as spatial priors, into the inverse scattering algorithm. We extend our previously presented spatial prior method to 3D and demonstrate its feasibility using high-fidelity numerical breast phantoms. The method exploits the fact that the dielectric properties of different types of tissues are distinct. The spatial prior method favors solutions to the inverse scattering problem that have small variations in dielectric properties within each spatial prior region. The amount of variation allowed in each of the regions is controlled by a single parameter that sets the strength of the spatial prior constraints. The extension to 3D is aided by the fact that this method uses sparse matrices and therefore is highly computationally efficient. We evaluate the performance of the algorithm in the presence of different levels of noise, and for different choices of the spatial prior strength controlling parameter. We also demonstrate the robustness of the algorithm with respect to imperfect spatial prior information.

1. Introduction

Microwave breast imaging via inverse scattering consists of reconstructing the dielectric properties of the breast from measurements of scattered electromagnetic fields *Shea et al.* [2010]. Microwave imaging offers several potential advantages compared to other breast imaging modalities such as X-ray mammography and MRI: it uses non-ionizing radiation, is low cost, and provides 3D tomographic images with quantitative information about tissue properties. This shows promise for several clinical applications, such as evaluation of breast density, detection of breast cancer, and monitoring of treatment.

However, resolution of microwave breast imaging via inverse scattering is typically moderate. To reconstruct the dielectric properties of the breast, it is required to solve a system of equations that has been linearized and is ill-posed. This requires regularization techniques that usually result in smooth, or blurred images. Attempts have been made to overcome the nonlinearity of the inverse scattering problem and improve image resolution while preserving boundaries [*van den Berg and Kleinman*, 1995; *Abubakar et al.*, 2002; *Mojabi and LoVetri*, 2009a, b; *Irishina et al.*, 2010]. However, this is still a remaining challenge.

An alternative to improve image resolution is to incorporate *a priori* structural information to the inverse scattering algorithm, also known as spatial priors. Structural information about the breast can be obtained from a different imaging modality, such as MRI, and then incorporated to the microwave inverse scattering algorithm to improve resolution and property estimation. Spatial prior methods exploit the

fact that the different types of tissues that constitute the breast (mainly adipose and fibroglandular tissue) have distinct dielectric properties, and therefore typically use mechanisms that favor solutions with high contrast between the tissues and/or penalize solutions with large variations within a tissue type. Spatial priors have been added to microwave breast imaging algorithms in *Golnabi et al.* [2013a] and *Golnabi et al.* [2013b]. In these cases, the spatial prior information was added to the inverse scattering problem in the form of soft constraints, and experiments in 2D for simple phantoms were reported. Furthermore, *Meaney et al.* [2013] presents a system for coregistration of MRI and microwave breast imaging, and tests it on actual patients using spatial priors.

In this paper we present a new method for incorporating spatial prior information to the microwave inverse scattering algorithm *Neira et al.* [2014]. Our method also uses soft spatial prior constraints, but concedes more flexibility than previously developed methods ([*Golnabi et al.*, 2013a, b]) in adjusting their weight, as they are not linked to the regularization of the problem. This allows a wider range of variation of the reconstructed properties in each of the regions provided by the *a priori* information.

Furthermore, our method is significantly computationally more efficient, as it stores the prior information in a sparse matrix. This is particularly useful and necessary when extending spatial prior methods to 3D.

We incorporate spatial prior information to the Distorted Born Iterative Method (DBIM) that is a conventional technique used to solve the inverse scattering problem *Chew* [1995]. We first evaluate the performance on 3D locally homogeneous breast

phantoms, to assess the accuracy of property estimation under simple conditions. Then, we test it on 3D realistic heterogeneous breast phantoms, obtained from the UW phantom repository *UWCEM Repository* [online], and study the effect of different levels noise in the measured data and different levels of weights for the spatial prior constraints. Finally, we evaluate the performance of the algorithm when there are errors in the prior information, in particular shifts in the location of the *a priori* known regions, and discuss what we can expect from the algorithm given other types of errors in the prior information.

The paper continues as follows. Section II provides a description of the conventional DBIM for inverse scattering and how we modified it to incorporate soft spatial prior constraints. Section III describes the simulation testbed and the phantoms we used for our tests. Section IV shows the results, and Section V discusses and evaluates the performance of the algorithm, and provides conclusions.

2. Method

We present an algorithm that incorporates spatial prior information to the distorted Born iterative method (DBIM) (though the same modifications can be applied to other inverse scattering methods). We first provide a brief description of DBIM (more detailed descriptions can be found in *Chew* [1995]), and then we describe how we modify conventional DBIM to incorporate spatial information.

2.1. Conventional DBIM

To reconstruct the dielectric properties of an object inside region V by measuring the electric fields outside the region, the DBIM attempts to solve the electric field integral equation:

$$\mathbf{E}^s(\mathbf{r}_{obs}) = \omega^2\mu \int_V \overline{\mathbf{G}}^b(\mathbf{r}_{obs}|\mathbf{r}')\mathbf{E}^t(\mathbf{r}')[\epsilon(\mathbf{r}') - \epsilon^b(\mathbf{r}')]d\mathbf{r}' \tag{1}$$

where $\mathbf{E}^s(r_{obs})$ is the scattered electric field, which is equal to the difference between the measured field and the incident field that is present given the background with dielectric profile $\epsilon_b(\mathbf{r})$, $\mathbf{G}^b(\mathbf{r}_{obs}|\mathbf{r}')$ is the dyadic Greens function for the background, $\mathbf{E}^t(\mathbf{r}')$ is the electric field inside the unknown region, and $\epsilon(\mathbf{r})$ is the dielectric profile of the unknown region.

In order to solve this equation, the DBIM linearizes the problem by setting $\mathbf{E}^t(\mathbf{r}')$ equal to the incident electric field, and discretizes the integral equation to form the system $\mathbf{Ax} = \mathbf{b}$, to find $\mathbf{x} = \epsilon(\mathbf{r}') - \epsilon^b(\mathbf{r}')$, which is the vector containing the contrast in each voxel inside the region V.

The solution $\mathbf{x}$ is then used to update the properties of the background, and the problem is solved again until the residual scattered fields are negligible (and the reconstructed dielectric properties of the scattering volume V are given by the updated background). Since the problem $\mathbf{Ax} = \mathbf{b}$ is ill posed, regularization techniques are required to keep the variables bounded. In previous studies, conjugate gradient least square error minimization with an early termination has been used for this purpose.

2.2. DBIM with spatial priors

DBIM with spatial priors (DBIM-SP) assumes we have prior information about the structure of the breast. In particular, it assumes we know the locations of different types of tissues, and that we can segment the breast into regions corresponding to the different tissues types. The breast consists mainly of two types of tissue: adipose and fibroglandular. DBIM-SP uses the fact that adipose and fibroglandular tissue have different electrical properties, but within a each type of tissue the properties vary only slightly *Lazebnik et al.* [2007].

In conventional DBIM we solve for the contrast $\mathbf{x}$ in each iteration, which is a vector that contains the contrasts of all the voxels in the scattering volume V. We would like to constraint those updates such that if two voxels belong to the same tissue type, or equivalently, to the same region, the update of the properties of the two voxels should be similar (assuming we start with a homogeneous background). This inspires solving an augmented system of equations, which in addition to solve the electric field equations, includes equations of the form $-x_i + x_j = 0$ if voxels i and j are in the same region.

Let us define this augmented system of equations as $\mathbf{A'x} = \mathbf{b'}$ where $\mathbf{A'} = [\mathbf{A}|\lambda\mathbf{M}]^T$, $\mathbf{b'} = [\mathbf{b}|\mathbf{0}]^T$, and $\mathbf{M}$ is of the form

$$\mathbf{M} = \|\mathbf{A}\| \cdot \left[\begin{array}{ccccc|ccccc} -1 & 1 & 0 & 0 & \cdots & 0 & 0 & 0 & 0 & \cdots \\ -1 & 0 & 1 & 0 & \cdots & 0 & 0 & 0 & 0 & \cdots \\ -1 & 0 & 0 & 1 & \cdots & 0 & 0 & 0 & 0 & \cdots \\ \vdots & \vdots & \vdots & \vdots & \ddots & \vdots & \vdots & \vdots & \vdots & \ddots \\ \hline 0 & 0 & 0 & 0 & \cdots & -1 & 1 & 0 & 0 & \cdots \\ 0 & 0 & 0 & 0 & \cdots & -1 & 0 & 1 & 0 & \cdots \\ 0 & 0 & 0 & 0 & \cdots & -1 & 0 & 0 & 1 & \cdots \\ \vdots & \vdots & \vdots & \vdots & \ddots & \vdots & \vdots & \vdots & \vdots & \ddots \end{array}\right] \tag{2}$$

if the first N voxels up to the vertical line are in one region, and the remaining voxels are in a second region. The norm of $\mathbf{A}$ is a scaling factor.

Note that this is an overdetermined system of equations and therefore it is likely to not have a solution that satisfies all equations, especially since in reality the tissues are heterogeneous. Therefore we solve this system of equations using conjugated gradient least square error minimization, which finds the solution that minimizes the error:

$$\|\mathbf{Ax} - \mathbf{b}\|^2 + \lambda^2\|\mathbf{Mx}\|^2. \tag{3}$$

We use the parameter λ to set the weight of the spatial prior constraints against the electric field matching equations. A large λ will put a large weight in ensuring the difference between two voxels in a region is small, and therefore will not allow variations of the properties within each region, while a small λ will give more importance to the matching of the electric field equations and the spatial prior constraints will result in soft constraints. As seen in equation 3, the matrix $\mathbf{M}$ is normalized so that a $\lambda = 1$ puts approximately equal importance to the matching of the electric field equations and the spatial prior constraints. A $\lambda > 1$ will give more importance

to the spatial prior constraints, and a $\lambda < 1$ will give more importance to the electric field equations.

To regularize the solution to the problem we terminate the conjugate gradient least square error minimization early. However, DBIM-SP needs less regularization than conventional DBIM because the spatial prior constraints help regularize the solution.

3. Models

3.1. Breast phantoms

We tested the algorithm on three numerical breast phantoms: a homogeneously dense phantom, a heterogeneously dense breast phantom, and a scattered fibroglandular breast phantom. We obtained the herogeneously dense breast phantom (Class 3, ID number 062204) and the scattered fibroglandular breast phantom (Class 2, ID number 010204) from the University of Wisconsin repository *UWCEM Repository* [online], and created the locally homogeneous phantom based on the Class 3 phantom. The locally homogeneous phantom is a thresholded version of the Class 3 phantom, which assumes the phantom is composed only by homogeneous adipose tissue and homogeneous fibroglandular tissue. Figure 1 shows the distribution of the properties of the three phantoms used.

The frequency dependent complex permittivities of the tissues in the phantoms were modeled using single-pole Debye models as in *Shea et al.* [2010]. *Shea et al.* [2010] fitted single-pole Debye models to measured data from *Zastrow et al.* [2008] for the properties of tissues in the interior of the breast and from *Gabriel et al.* [1996]

for the properties of the skin, on the frequency range of 0.5-3.5 GHz. The skin was considered to be homogeneous and was given a thickness of 2 mm.

3.2. Simulation set-up

The simulation setup consisted of an array of forty dipoles surrounding different breast phantoms, all immersed in a lossless medium (ϵ_r). The dipoles were positioned vertically (z polarized) and were arranged in a cylindrical surface into five coronal rings surrounding each breast phantom, with a minimum distance of 1 cm to the skin surface of the phantom. The rings were positioned equally spaced along the axial extent of the phantom, and they were rotated with respect to adjacent rings to maximize the distance between the dipoles.

Fields were simulated using the FDTD method, taking each dipole as a source and observation points. FDTD simulations were run individually for each source, and electric field measurements were recorded at the remaining dipoles. A modulated Gaussian pulse was used to excite the dipoles, and the measurements were transformed to the frequency domain and recorded at 1, 1.5, 2, and 2.5 GHz.

For the simulation of the acquisition of the measurements, we used FDTD in a 0.5 mm grid. To calculate the Green's function and the incident fields inside the imaging region in each iteration, we discretized the setup further to a 2 mm grid. The properties of the immersion medium, the properties of the skin, and the location of the phantoms were considered known, and therefore in each iteration only the properties in the interior of the phantoms were updated.

3.3. Spatial priors

Figure 2 shows the two regions used as spatial prior in the DBIM-SP for each phantom. The black region corresponds to adipose tissue and white region corresponds to fibroglandular region. The regions were formed by using a threshold on the phantom's properties that would give us an appropiate separation of the two tissue types (the threshold was a static relative permittivity above/below 18).

Note that because the data acquisition takes place in a 0.5 mm grid, and the reconstruction in a 2 mm grid, the spatial prior regions do not match the phantom exactly.

4. Results

4.1. Locally homogeneous phantom

As presented in the models section, the locally homogeneous breast phantom consists of two distinct homogeneous tissues: adispose and fibroglandular. Figure 3 shows the dielectric properties of the two tissues across the frequency range of interest, along with the estimation of these properties using DBIM-SP with a large λ ($\lambda = 5$). A large λ was chosen to minimize variations of the properties inside each region allowing us to assess the accuracy of the estimation of the properties. We can see that the estimation of the relative permittivity and effective conductivity is accurate for all frequencies using DBIM-SP, both for the adipose and fibroglandular tissues.

4.2. Heterogeneously dense breast phantom

Figure 4 shows coronal, sagittal, and axial views of the relative permittivity at 1 GHz of the class 3 breast phantom (first row) and three different reconstructions for a 30 dB SNR: conventional DBIM (second row), DBIM-SP with large λ ($\lambda = 50$), and DBIM-SP with a small λ ($\lambda = 0.5$). The reconstruction with conventional DBIM suffers from blurred edges between the different tissues and poor property estimation, especially underestimating the relative permittivity of the fibroglandular tissue. In contrast, DBIM-SP preserves the edges between the different tissues, and is more accurate in the estimation of the properties. When using a large lambda (third row), no variation of the properties is allowed in each region, and the reconstruction consists of two locally homogeneous regions, each with properties close to the average properties of the tissues in the original phantom (average ϵ_r at 1GHz of phantom/reconstruction: 6/5 in adipose and 43/45 in fibroglandular tissue). When using DBIM-SP with a small lambda (fourth row), the boundaries are still well preserved between the tissues, but the reconstruction captures some of the heterogeneity of the tissues. We can appreciate this more clearly in Figure 5, which shows cumulative distributions of the properties of each region (plot (a) shows adipose region, and plot (b) shows fibroglandular region) for the original phantom, conventional DBIM, and several reconstructions using DBIM-SP with different values of λ.

In Figure 5 we can clearly see how DBIM overestimates the relative permittivity of the adipose tissue and underestimates the properties of the fibroglandular tissue. Also, note that cumulative distributions for DBIM are very smooth and flat compared

to the cumulative distribution of the properties of the original phantom. This is because DBIM is smoothing the variation of the properties inside the imaging region and the boundaries between different tissue types are blurred. By inspecting the cumulative distributions of the reconstructions using DBIM-SP we can see the effect of different values for λ. In particular note that a $\lambda = 50$ results in no variation inside each region, and as we decrease λ variations inside each region are allowed, until for a $\lambda = 0.05$ the reconstruction performs similar to DBIM.

Figure 6 and Figure 7 show the cross sections and cumulative distributions of the relative permittivity at 1 GHz of the phantom and the reconstructions when the measured fields have a low SNR (SNR= 10 dB). Note that the reconstruction using DBIM completely breaks down at this level of noise (Figure 6, second row), while DBIM-SP continues to perform well. The cumulative distribution of DBIM is nearly flat at high noise, while the performance of DBIM-SP barely changes compared to a low level of noise, even small values of λ.

The results for the Class 2 scattered fibroglandular breast phantom show a similar performance. This phantom has larger volume than the Class 3 phantom, and consists of mostly adipose tissue with a few scattered regions of fibroglandular tissue. DBIM-SP estimates the average properties of the tissues accurately and when using a small λ, heterogeneity can be captured.

4.3. Errors in prior information

In this section we provide the setup and results for how DBIM-SP performs when the prior information is not exactly correct. Up to now we have only considered a

mismatch given by the discretization of the imaging region. Now we will considered shifts in the spatial prior. Viewing the phantom from the top (coronal view), we will consider shifts to the right and to the left of the fibroglandular region in the DBIM-SP reconstructions of the class 3 phantom (heterogeneously dense), using a small λ for the spatial prior constraints.

Figure 8 shows coronal cross sections of the class 3 phantom (first row) and its reconstructions using DBIM-SP. The second row shows the reconstruction with the correct location of the fibroglandular region in the prior, the third row uses a prior which has the fibroglandular region shifted 4 mm shift to the right, and the fourth row uses a prior that has the fibroglandular region shifted 4 mm shift to the left. The second and third columns show the reconstruction of just the adipose tissue and fibroglandular tissue. Note that when the location of the spatial prior is correct, we obtain the result previously shown in Figure 4, the boundaries are well preserved and the estimation of the average properties in each region is accurate, while still capturing some of the heterogeneity in each region. When shifts in the priors are introduced, the estimation of the properties tries to compensate for the errors in the prior, both by introducing variations of the mismatched tissues inside each region and changing the average properties of each region. In the third row (prior shifted to the right) we see that the estimation of the left edge of the fibroglandular region is increased compared to when there were no errors. Also, the estimated properties of the adipose tissue surrounding that edge are higher. This is trying to compensate for the fact that that is fibroglandular tissue in the phantom. In the fourth row (prior

shifted to the left) we can see a similar effect: the left edge of the fibroglandular region has lower properties, because it corresponds to adipose tissue in the phantom.

Table 1 shows the average properties of the fibroglandular and adipose tissues in the phantom and in the reconstructions: conventional DBIM, DBIM-SP without errors in the prior, and DBIM-SP with different amounts of errors/shifts in the prior. An interesting result is that the estimation of the average properties of each tissue type is still accurate for small errors in the prior. Also note that DBIM-SP with errors in the prior performs better than DBIM at estimating the average properties of each tissue for up to a 6 mm error in the prior.

5. Discussion and Conclusions

The implementation of the DBIM-SP in 3D was possible because the method uses sparse matrices, which makes possible to store and perform mathematical operations with the data efficiently. The number of unknown voxels in each phantom was on the order of 40,000 for the locally homogeneous and heterogeneously dense phantoms (Class 3), and of 65,000 for the scattered fibroglandular phantom (Class 2), which results in 120 thousand and 195 thousand unknowns respectively (three unknown Debye parameters per voxel). Therefore, the matrix M in DBIM-SP has dimensions close to 120 thousand and 195 thousand rows and columns, respectively for each phantom. Storing and operating these matrices is achievable because they are highly sparse (they only have two non-zero elements in each row). This characteristic is not present in the spatial prior algorithms presented in [*Golnabi et al.*, 2013a, b; *Meaney*

et al., 2013], and we see this as a clear benefit of our algorithm, which made the extension to 3D feasible.

The method performs substantially better than the conventional DBIM at estimating the average properties of the tissues in the phantoms. In fact, it achieves almost exact property estimation when the phantom consists of locally homogeneous tissues. We also saw that the estimation of the average properties is good even in the presence of noise for all phantoms and even when there were relatively large errors in the spatial prior regions.

By controlling the parameter λ we allowed for different levels of variations in the estimated properties inside each region. In the plots of cumulative distributions of the actual and estimated properties of the phantoms, we saw that a large λ acted as a hard constraint, and that by decreasing λ the estimation of the properties began to follow the heterogeneity of the actual properties of the phantoms. In other spatial prior algorithms that implement soft constraints *Golnabi et al.* [2011], the parameter that sets the weight of the spatial prior constraints is linked to the regularization of the problem, and therefore the solutions diverge for very small values of the parameter making it not possible to obtain a significant amount of variation inside each region. In the DBIM-SP method, a tiny λ will perform like conventional DBIM, and several different amounts of variation can be obtained between DBIM and the hard constraint by choosing intermediate λ's. However, the variations inside each region result to be very smooth. Further research in the proper choice or adaptive choice of λ could give us results with even higher resolution.

Allowing variations inside each region is also of special importance to handle errors in the prior. We saw that when there are errors in the location of the spatial prior regions the algorithm compensates the error by correcting the estimation of the average properties in the regions, and also compansates for the errors by raising/lowering the properties in the parts of the regions that are mismatched with the actual phantom. It would be interesting to look at the possibility of adapting the spatial prior regions if this effect becomes present in the estimation of the properties.

The DBIM-SP compensates in very simple and intuitive ways for errors in the prior, and therefore we can easily predict ots performance when there are other types of errors in the prior information. For example, if there is we set a false inclusion as a third region immersed in the adipose tissue, the method will still image it as adipose tissue, as it will estimate its properties to be close to the average properties of the background at that location. If we create a false inclusion in the adipose tissue that is linked to the fibroglandular region (so we still only have 2 regions) the algorithm will change the average properties of each region to compensate, and if a small λ is chosen, it will also lower the estimated properties of the false inclusion compared to the average of that region.

References

UWCEM, [online]. available: http://uwcem.ece.wisc.edu, university of wisconsin computational electromagnetics laboratory, uwcem numerical breast phantom repository.

Abubakar, A., P. M. van den Berg, and J. J. Mallorqui (2002), Imaging of biomedical data using a multiplicative regularized contrast source inversion method, *IEEE Trans. Microw. Theory Tech.*, *50*(7), 1761–1771.

Chew, W. (1995), *Waves and Fields in Inhomogeneous Media.*, IEEE Press, Piscataway, NJ.

Gabriel, S., R. W. Lau, and C. Gabriel (1996), The dielectric properties of biological tissues: Iii. parametric models for the dielectric spectrum of tissues, *Phys. Med. Biol.*, *41*, 2271–2293.

Golnabi, A. H., P. M. Meaney, S. D. Geimer, and K. D. Paulsen (2011), Comparison of no-prior and soft-prior regularization in biomedical microwave imaging, *J. of Med. Phys.*, *36*(3), 159–170.

Golnabi, A. H., P. M. Meaney, and K. Paulsen (2013a), Tomographic microwave imaging with incorporated prior spatial information, *IEEE Trans. Microw. Theory Tech.*, *61*(5), 2129–2136.

Golnabi, A. H., P. Meaney, S. D. Geimer, and K. D. Paulsen (2013b), Comparison of no-prior and soft-prior regularization in biomedical microwave imaging, *J. Med. Phys.*, *36*(3), 159–170.

Irishina, N., D. Alvarez, O. Dorn, and M. Moscoso (2010), Structural level set inversion for microwave breast screening, *Inverse Probl.*, *26*(3), 035,015.

Lazebnik, M., L. McCartney, D. Popovic, C. B. Watkins, M. J. Lindstrom, J. Harter, S. Sewall, A. Magliocco, J. H. Booske, M. Okoniewski, and S. C. Hagness (2007), A large-scale study of the ultrawideband microwave dielectric properties of normal

breast tissue obtained from reduction surgeries, *Phys. Med. Biol.*, *52*, 2637–2656.

Meaney, P. M., A. H. Golnabi, N. R. Epstein, S. D. Geimer, M. W. Fanning, J. B. Weaver, and K. D. Paulsen (2013), Integration of microwave tomography with magnetic resonance for improved breast imaging, *Med. Phys.*, *40*(10), 103,101.

Mojabi, P., and J. LoVetri (2009a), Overview and classification of some regularization techniques for the gauss-newton inversion method applied to inverse scattering problems, *IEEE Trans. Antennas Propag.*, *57*(9), 2658–2665.

Mojabi, P., and J. LoVetri (2009b), Enhancement of the krylov subspace regularization for microwave biomedical imaging, *IEEE Trans. Med. Imag.*, *28*(12), 2015–2019.

Neira, L. M., B. D. V. Veen, and S. C. Hagness (2014), An inverse scattering algorithm with spatial prior constraints for high-resolution microwave breast imaging, *Proc. 2014 IEEE International Symp. Antennas and Propagation*, pp. 1113–1114.

Shea, J. D., P. Kosmas, S. C. Hagness, and B. D. V. Veen (2010), Three-dimensional microwave imaging of realistic numerical breast phantoms via a multiple-frequency inverse scattering technique, *Med. Phys.*, *37*(8), 4210–4226.

van den Berg, P. M., and R. E. Kleinman (1995), A total variation enhanced modified gradient algorithm for profile reconstruction, *Inverse Probl.*, *11*(3), LS–L10.

Zastrow, E., S. K. Davis, M. Lazebnik, F. Kelcz, B. D. V. Veen, and S. C. Hagness (2008), Development of anatomically realistic numerical breast phantoms with accurate dielectric properties for modeling microwave interactions with the human breast, *IEEE Trans. Biomed. Eng.*, *55*(12), 2792–2800.

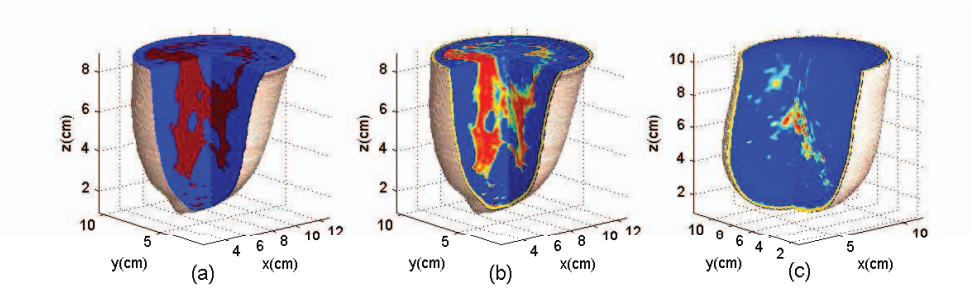

Figure 1. Distribution of dielectric properties of breast phantoms. (a) Locally homogeneous phantom, (b) heterogeneously dense phantom (Class 3), and (c) scattered fibroglandular phantom (Class 2).

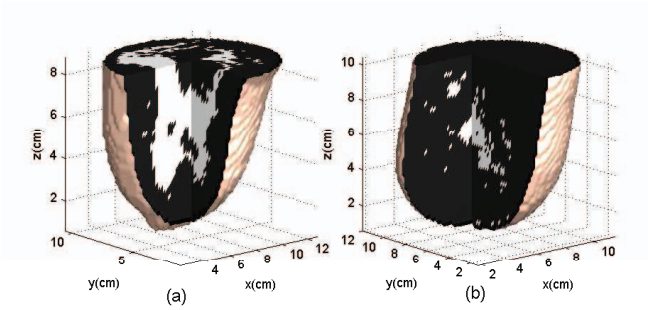

Figure 2. Spatial prior regions considered for each phantom. Black corresponds to adipose region, and white corresponds to fibroglandular region. (a) Regions for locally homogeneous and heterogeneously dense phantoms. (b) Regions for scattered fibroglandular phantom.

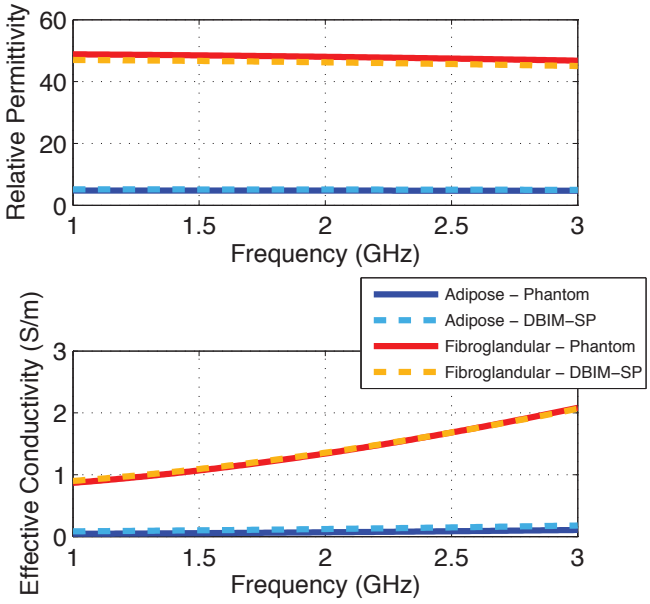

Figure 3. Comparison of the actual (solid) and DBIM-SP reconstructed (dashed) dielectric properties in the adipose (light/dark blue) and fibroglandular (red/orange) tissue regions in a locally homogeneous breast phantom.

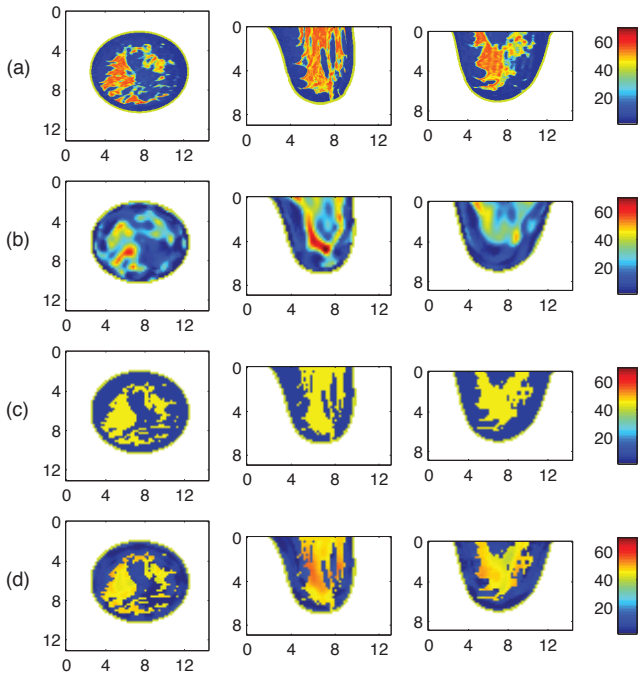

Figure 4. Coronal (left column), sagittal (middle column), and axial (right column) cross-sections of the relative permittivity at 1 GHz for the (a) Class 3 breast phantom, (b) standard DBIM reconstruction, (c) DBIM-SP reconstruction ($\lambda = 50$), and (d) DBIM-SP reconstruction ($\lambda = 0.5$). All reconstructions were obtained for 30 dB SNR. (Axes in cm.)

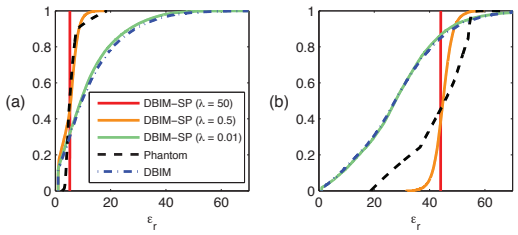

Figure 5. Cumulative distributions of the relative permittivity at 1 GHz for Class 3 reconstructions with 30 dB SNR. (a) Adipose tissue. (b) Fibroglandular tissue.

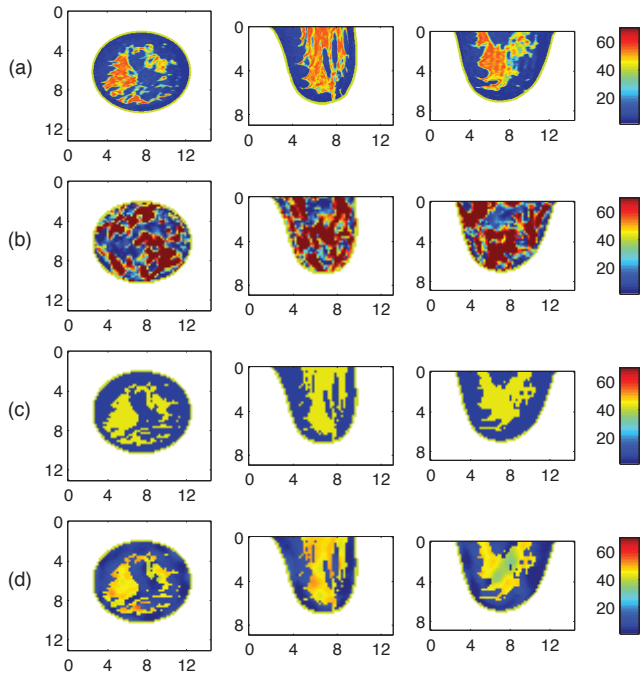

Figure 6. Coronal (left column), sagittal (middle column), and axial (right column) cross-sections of the relative permittivity at 1 GHz for the (a) Class 3 breast phantom, (b) standard DBIM reconstruction, (c) DBIM-SP reconstruction ($\lambda = 50$), and (d) DBIM-SP reconstruction ($\lambda = 0.5$). All reconstructions were obtained for 10 dB SNR. (Axes in cm.)

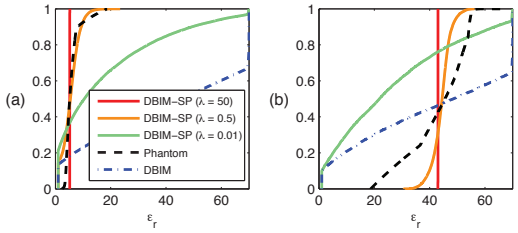

Figure 7. Cumulative distributions of the relative permittivity at 1 GHz for Class 3 reconstructions with 10 dB SNR. (a) Adipose tissue. (b) Fibroglandular tissue.

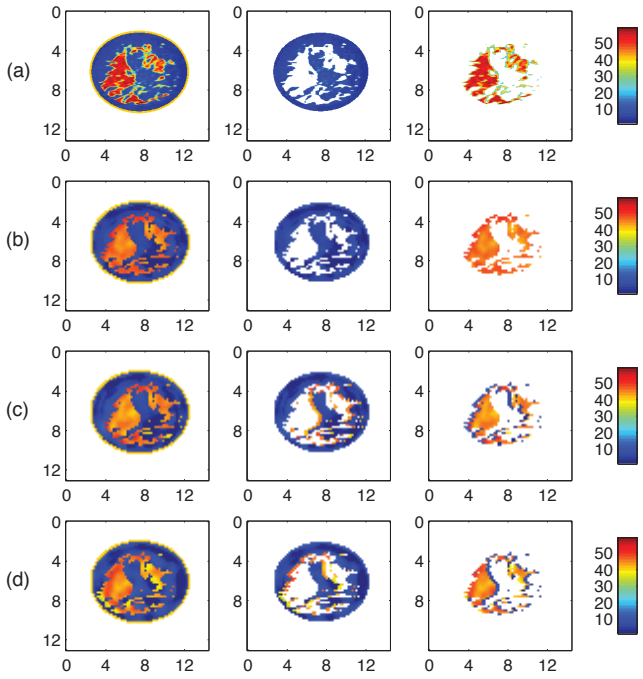

Figure 8. Coronal cross-sections of the relative permittivity at 1 GHz for the (a) Class 3 breast phantom, (b) DBIM-SP reconstruction without errors in prior, (c) DBIM-SP reconstruction with 4 mm error in prior to the right, and (d) DBIM-SP reconstruction with 4 mm error in prior to the left. The middle and right columns show only the adipose tissue and fibroglandular tissue regions, respectively. All reconstructions were obtained for 30 dB SNR and $\lambda = 0.5$. (Axes in cm.)

Table 1. Average relative permittivity of tissues at 1 GHz

	Phantom	DBIM	DBIM-SP no errors
Adipose	5.9	12.8	5.0
Fibroglandular	42.9	28.2	45.3

	DBIM-SP with prior shifted to the left (L) and right (R)							
	8 mm L	6 mm L	4 mm L	2 mm L	2 mm R	4 mm R	6 mm R	8 mm R
Adipose	10.8	10.8	10.4	8.2	8.3	10.4	11.0	11.0
Fibroglandular	26.2	28.0	31.3	37.9	37.2	31.5	28.6	26.4

College of Engineering
UNIVERSITY OF WISCONSIN-MADISON

Professor Erdem Topsakal
Mississippi State University

March 23, 2015

Dear Prof. Topsakal:

We are writing to clarify the roles of the co-authors on the following paper that our student, Luz Maria Neira, is submitting to the USNC-URSI Student Paper Competition:

Title: "Investigation of High-Resolution Microwave Breast Imaging using a 3-D Inverse Scattering Algorithm with a Variable-Strength Spatial Prior Constraint"

Authors: Luz Maria Neira, Barry D. Van Veen, and Susan C. Hagness

Ms. Neira is a Ph.D. student at the University of Wisconsin-Madison. We are formally serving as her dissertation co-advisors, and our contribution to the paper under question has been solely advisory in nature.

Sincerely,

Susan C. Hagness
Philip D. Reed Professor

Barry D. Van Veen
Lynn H. Matthias Professor

Department of Electrical and Computer Engineering, University of Wisconsin-Madison
1415 Engineering Drive, Madison, WI 53706 USA
Voice: 608-265-5739 Fax: 608-262-1267 E-mail: hagness@engr.wisc.edu